ACS APPLIED MATERIALS & INTERFACES

www.acsami.org

Research Article

Spontaneous Graphene/Lipid Bicellar Co-assembly (NANO^2-Graphene): Experiments and Computer Simulations

Donyeil Hoy, Jr.,[¥] Yiyan Kuang,[¥] Alemayehu Asres, Chung-Hao Liu, Elena Dormidontova,* and Mu-Ping Nieh*

Cite This: *ACS Appl. Mater. Interfaces* 2025, 17, 66221−66234

Read Online

ACCESS | Metrics & More | Article Recommendations | Supporting Information

ABSTRACT: Using a combined experimental and computer modeling approach, we demonstrate that graphene can self-assemble with a discoidal lipid bicelle, forming a graphene incorporated nanodisc structure (NANO^2-graphene) over a wide range of graphene-to-lipid ratios (from 1:2000 to 1:40 by weight). Structural characterization via dynamic light scattering (DLS), differential scanning calorimetry (DSC), and small-angle X-ray scattering (SAXS) confirms the encapsulation of graphene in the bicelles and suggests that the presence of graphene enhances the stability of the discoidal structure and prevents the usual thermally induced bicelle-to-vesicle transition. Both molecular dynamics (MD) simulations and DSC results show that bicelles are capable of encapsulating a significant graphene content and that the graphene incorporation significantly suppresses the lipid ordered phase and decreases lipid lateral diffusion. MD simulations also reveal that, in the presence of single or stacked graphene layers, lipid tails bend and orient along the graphene surface to maintain the bilayer thickness with the lipid order parameter significantly reduced and the area per lipid increased along with water contacts with lipid headgroups. These results provide important insights into the interaction between lipid molecules and graphene that should be considered in the biomedical application of graphene-containing nanomaterials and, more broadly, the effect of graphene on lipid-containing biointerfaces.

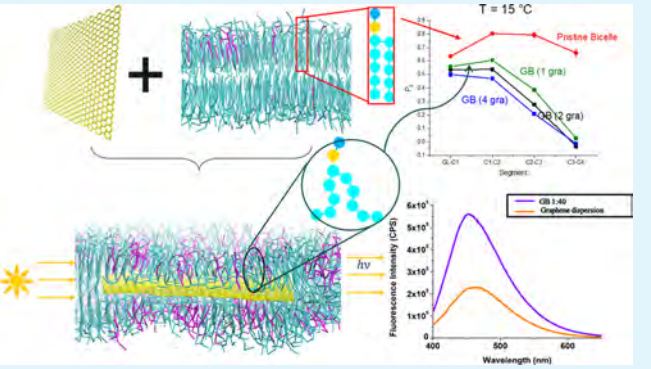

KEYWORDS: *lipid nanodiscs, bicelle, molecular dynamics, graphene encapsulation, aggregation enhanced emission, SAXS, DSC*

INTRODUCTION

Graphene is the thinnest known material, composed of only a single 2D sheet of sp^2 hybridized carbon atoms arranged in a honeycomb lattice structure. It can be produced through the exfoliation of bulk graphite by mechanical, thermal, electrochemical, and intercalative means. Since its isolation from graphite in 2004, graphene has been intensely studied due to its unique physicochemical properties[1] including high mechanical strength and excellent electrical and thermal conductivity.[2] It also has a large specific hydrophobic surface area allowing it to efficiently load hydrophobic drugs and other small molecules, suggesting significant potential as a drug delivery agent.[2,3] In biophysics, it is also of great interest to understand how such a 2D hydrophobic object interacts with a lipid bilayer. Furthermore, graphene oxide can serve as a potential diagnostic agent owing to its fluorescence property (also known as a "carbon dot"). While graphene has many desirable unique properties, its hydrophobicity leads to aggregation in aqueous and physiologically relevant environments, affecting its biomedical applications.[4] Similarly, graphene can also adhere nonspecifically to tissues long before reaching a targeted site, limiting bioavailability and overall therapeutic efficacy.[5,6] Simulation studies have shown that coating graphene with phospholipids reduced their ability to penetrate lipid bilayers.[7] This suggests that graphene encapsulation in lipid carriers may lead to a reduction in undesired cell membrane interactions, thereby reducing toxicity and improving therapeutic efficacy.

One of the model biomembranes is the discoidal bicelle, which is generally constructed by a long-chain (with 12 carbons or greater in acyl-chain length) lipid bilayer with the rim belted by other amphiphilic species such as short-chain lipids (with seven carbons or less in acyl length), detergents (bile salts or acids), membrane scaffold protein (MSP), or amphiphilic polymers (e.g., styrene-maleic acid).[8−15] The short-chain lipid mediated bicelles normally have a uniform size with a radius of 10−20 nm and thickness of 5 nm. It has

Received: June 23, 2025
Revised: November 10, 2025
Accepted: November 11, 2025
Published: November 25, 2025

been reported that low-temperature discoidal bicelles at high lipid concentration can be transformed into perforated lamellae or bilayered ribbons upon elevated temperature,[13−15] leading to a magnetically alignable phase, facilitating the *in situ* structural analysis of membrane-associated proteins via pseudo-solid-state nuclear magnetic resonance (NMR) in solution.[8] More recently, bicelles have been demonstrated to be effective carriers for the delivery of small molecular species, such as diclofenac diethylamine, β-carotene, gold nanoclusters (NANO^2-Au nanoclusters), quantum dots (NANO^2-QD), nucleic acid, and doxorubicin, among others.[16−26] They have also been used for the delivery of monomeric fullerenes for photodynamic therapy, the only reported bicellar delivery of a carbon family material to date.[27]

Extensive simulation studies on the interaction between a graphene nanosheet and lipid membrane have been reported. Early molecular dynamics (MD) simulation suggested that graphene can be stabilized by the hydrophobic environment of lipid tails.[28] Some simulation studies focus on the mechanism of entry of a graphene nanosheet into a lipid bilayer,[29−32] including the role of angle and orientation of graphene insertion into a bilayer[29−31] and how cholesterol in a bilayer[32] affects the entry mechanism. Another study on the morphological variation of lipid bilayers on graphene or graphene oxide has found that the lipid order is greatly reduced due to the lateral interactions between lipid tails and surfaces and that the diffusion of lipids becomes slower in the presence of graphene.[33] Additionally, an experimental report on graphene encapsulation in a lipid bilayer has demonstrated phospholipid-assisted exfoliation of graphite in an aqueous environment,[34] in which the lipids rapidly desorbed from graphene, resulting in lipid vesicles (liposomes) and the aggregation of graphene.

As an investigation on the interactions between graphene and lipid bilayers offers valuable insight into the cellular uptake of graphene and rational design of graphene-derived lipid nanoparticles, this report will demonstrate that stable size-uniform graphene-encapsulating bicelles (nanographene in nanodiscs, denoted herein as NANO^2-graphene) are attainable. We have used dynamic light scattering (DLS), small-angle X-ray scattering (SAXS) data, and differential scanning calorimetry (DSC) thermograms to investigate the structures of NANO^2-graphene and the conformation of lipids after graphene encapsulation. MD simulations have been performed to characterize the lipid order parameter in the presence of graphene sheet(s) entrapped in the middle of the bilayer and yield outcomes consistent with the experimental outcomes.

EXPERIMENTAL SECTION

Materials. 1,2-dihexanoyl-*sn*-glycero-3-phosphocholine (DHPC), 1,2-dipalmitoyl-*sn*-glycero-3-phosphocholine (DPPC), and 1,2-dipalmitoyl-*sn*-glycero-3-phospho-(1′-rac-glycerol) (sodium salt) (DPPG) were purchased from Avanti Polar Lipids, Inc. (Alabaster, AL). The DPPC and DHPC stock solutions were prepared by dissolving each lipid in chloroform, while the DPPG stock solution was prepared using a 65% chloroform and 35% methanol solution. Nano24 graphite was purchased from Asbury Graphite Mills (Kittanning, PA). 1-Methyl-2-pyrrolidinone (NMP) was purchased from Sigma-Aldrich (St. Louis, MO). Chloroform and methanol were purchased from Fisher Scientific (Waltham, MA).

Sample Preparation. *Preparation of Graphene Dispersion.* A graphene dispersion was prepared from the exfoliation of submicron graphite in NMP using the procedure described by Khan et al.[35] Graphite powder (1.65 g) was added to a flask containing 500 mL of NMP. The flask was placed in a sonicator bath for 168 h to produce a graphene dispersion. The dispersion was then centrifuged at 50,000*g* for 30 min, and the precipitate was discarded. This step was repeated four times to reduce the fraction of unencapsulated graphene. It should be mentioned that nanosized graphene is also attainable commercially, while we are able to make graphene or low-stacking graphite in large quantities through this method.

Preparation of Pristine Bicelles. Bicelles were prepared according to the standard published method in the literature.[16,21,22,24,25] The short-chain lipid DHPC, the long-chain lipid DPPC, and the charged long-chain lipid DPPG were mixed with a molar ratio of long-chain to short-chain lipids (Q, as defined below) = 3 and a molar ratio of charged to total long-chain lipid (R, as defined below) = 0.01 or 0.05, respectively, to a final lipid mass of 10 mg. Charged DPPG was added in the mixture to inhibit possible fusion between bicelles.[36]

$$Q = \frac{[\mathrm{DPPC}] + [\mathrm{DPPG}]}{[\mathrm{DHPC}]}; \quad R = \frac{[\mathrm{DPPG}]}{[\mathrm{DPPC}] + [\mathrm{DPPG}]}$$

The lipid mixture was then placed on a hot plate at 50 °C under nitrogen to remove the chloroform and methanol. The resultant lipid film was vacuumed at 80 °C for 5 days to completely remove solvent. The dry mixture was hydrated with 100 μL of filtered water and temperature-cycled above (>60 °C) and below (<5 °C) the lipid melting transition temperature (T_m) eight times with vortex to yield a 10 w/v% bicelle stock solution.

Preparation of Graphene-Loaded Bicelles (GB). Lipid mixtures were prepared with Q = 3 and R = 0.01 or 0.05, respectively, at a final lipid mass of 10 mg. Then, aliquots of the graphene dispersion were added to each lipid mixture with various graphene/lipid mass ratios (i.e., 1:2000, 1:1000, 1:667, 1:500, 1:200, and 1:40). The resultant mixtures were then vortexed and placed directly into a vacuum oven at 80 °C for 5 days to remove the NMP solvent. The weight of the dried samples was continuously monitored to ensure the complete removal of NMP (i.e., no further reduction of the weight with a longer drying process). In general, 4 days of the drying process is sufficient. The mixtures were rehydrated in water to form a lipid concentration of 10 w/v% aqueous solutions and then temperature cycled as described above. The final GB solutions were then centrifuged at 21,000 relative centrifugal force for 30 min to remove unencapsulated graphene or large aggregates. The supernatants were the final GB samples for further characterization. This procedure can be applied to manufacturing solid GB or highly concentrated GB solutions and further diluted to low-concentration GB solutions on demand for large-scale, high-stability production, defraying the cost for long-distance transportation.

Simulation. *Coarse-Grained Molecular Dynamics Simulation.* The coarse-grained molecular dynamics (CGMD) simulations were performed with the MARTINI 2 force field.[37] The MARTINI is a coarse-grained (CG) force field successfully used for molecular dynamics simulations of biomolecular systems and, in particular, lipid bilayers.[37,38] The MARTINI CG model is able to reproduce the self-assembly process of lipid bilayers and structural properties such as the area per lipid headgroup and bilayer thickness that are in a good agreement with the experimentally measured values.[37,39] However, the temperature at which the lipid (gel-to-liquid) phase transition occurs in MARTINI coarse-grained simulations is somewhat lower than the experimental phase transition temperature,[36,38,40−42] which is believed to be due to the coarse-grained nature of molecular dynamics simulations.[37,38,43] Although the direct numerical comparison between the experiment and simulation of the lipid gel−liquid transition temperature may not be feasible, the relative change in the transition temperature upon modification of bilayer, e.g., by graphene presence, can be readily assessed and compared with experimental results. The force field for graphene is adapted from the literature.[44] We created a new type of bead named GR to follow the 4:1 mapping for carbon atoms of a graphene sheet, and the GR-type bead has the same size and mass as the the MARTINI C1-type bead.[37] The bonds, angles, dihedrals, and nonbonded self-interaction parameters are taken from the model, and the nonbonded interaction parameters with all other types of beads are the same as for C1-type bead, which

https://doi.org/10.1021/acsami.5c11189
ACS Appl. Mater. Interfaces 2025, 17, 66221−66234

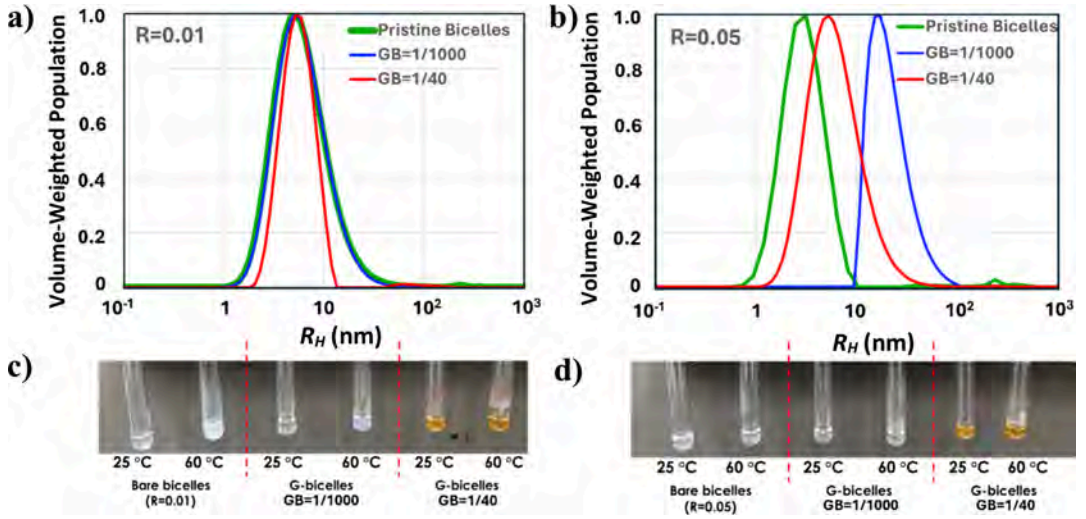

Figure 1. Hydrodynamic radius (volume-weighted) of 0.1 w/v% pristine bicelles (dark yellow) and GB 1:1000 and GB 1:40 (blue and pink, respectively) with (a) low charge (Q = 3, R = 0.01) and (b) high charge (Q = 3, R = 0.05). The physical appearance of (c) R = 0.01: pristine bicelles, GB = 1/1000, GB = 1/40 and (d) R = 0.05: pristine bicelles, GB = 1/1000, GB = 1/40 at 25 and 60 °C, respectively.

has been proven to be valid in previous research.[44,45] The main improvement of this improved graphene model is that it also correctly reproduces the experimental spacing of 0.335 nm between adjacent layers of graphene sheets.[46]

The models consisted of 960 DPPC and 320 DHPC molecules with one, two, or four 10 × 10 nm^2 graphene sheets. The graphene sheet(s) was(were) placed in the middle of the simulation box with half of the mixed phospholipids placed below the graphene sheet while the other half was above. Then, the simulation box was filled with CG water (each CG water bead representing four water molecules) with about 8% of the total water beads being larger antifreeze water beads to prevent the system from freezing at lower temperature.[37] The system was first equilibrated for 2 ns, and then the NPT simulations were performed at four different temperatures, i.e., 288, 293, 298, and 308 K, for 1000 ns with a time step of 0.002 ps. The simulations were coupled to a Berendsen thermostat (lipids, graphene, water, and antifreeze water were coupled separately to Berendsen heat baths with a coupling time constant of 1 ps). Pressure coupling was carried out with a time constant of 2 ps and compressibility of 3 × 10^{-5} bar^{-1} using a Berendsen barostat at 1 atm pressure. A cutoff distance of 1.2 nm was used for the van der Waals interactions with the Lennard−Jones potential and electrostatic interactions with a Coulombic potential. All simulations were performed using the 2016.3 GPU version of GROMACS for consistency with previous work.[47] All visualizations of systems were produced by the Visual Molecular Dynamics (VMD) software package.[48]

Experimental Methods. *Dynamic Light Scattering (DLS) Experiments.* DLS experiments were performed at an ALV Compact Goniometer System with multidetectors (CGS-3MD, Germany) equipped with a 22 mW 632.8 nm He−Ne laser. The autocorrelation function is collected with an ALV-7004 digital multiple tau real-time correlator. Samples were prepared from the bicelle and GB stock solutions at a lipid concentration of 0.1 w/v%. All data were collected at θ = 90°. From the characteristic relaxation time, the diffusion coefficients of the particles can be obtained. The hydrodynamic radius R_H can be further derived using the Stokes−Einstein relationship.

UV/Visible (UV/Vis) Spectroscopy. UV/vis absorption spectra were conducted using a PerkinElmer Lambda 1050 instrument with a tungsten halogen light source and a three-detector module for photomultiplier tube, InGaAs, and PbS detection. The samples were loaded into standard borosilicate glass cuvettes with a 10 mm path length. Data were collected over a wavelength range from 200 to 800 nm. Samples were measured at a lipid concentration of 0.1 w/v%.

Fluorescence Spectroscopy. The 1D and 2D fluorescence experiments were performed on a steady-state Horiba Fluorolog III with a 450 W short arc xenon lamp. The samples were loaded into standard borosilicate glass cuvettes with a 10 mm path length. For the 1D experiments, samples were excited at 380 nm, and emission data were collected from 400 to 660 nm with a 5 nm slit size. For the 2D experiments, the samples were excited from 310 to 500 nm, and emission data were collected from 300 to 650 nm with a 1 nm slit size. First- and second-order Rayleigh masking was enabled for the 2D experiments. Samples were measured at a lipid concentration of 0.1 w/v%.

Differential Scanning Calorimetry (DSC). DSC experiments were performed using a NanoDSC instrument from TA Instruments (New Castle, DE). Samples were analyzed at a lipid concentration of 0.1 and 1 w/v%. The temperature range was set from 5 to 60 °C with a scan rate of either 1 or 2 °C/min. The equilibration time between the heating and cooling scans was 10 min. Peaks were analyzed for enthalpy calculations by using Origin Pro 8.5.

Small-Angle X-ray Scattering (SAXS) Experiments. SAXS experiments were conducted at the Brookhaven National Laboratory National Synchrotron Light Source-II (NSLS-II) using the Life Science X-ray (16ID-LiX) beamline with an X-ray energy of 13.5 keV. Scattering data were collected on three individual pixel array detectors with overlapping scattering angles to cover a continuous range of scattering vector q ($q = \frac{4\pi}{\lambda}\sin\frac{\theta}{2}$, where θ is the scattering angle and λ is the wavelength of the X-ray) from 0.005 to 2.665 $Å^{-1}$. The useful q range for data fitting was 0.005 to 0.6 $Å^{-1}$ due to the influence of the sharp water peak. The samples were diluted to a lipid concentration of 1.0 w/v% and loaded into a 14-cell sample holder wedged between two mica sheets with a cell thickness of 1.0 mm. The sample holder was placed on a temperature control stage, and data were collected at 25 and 60 °C. The 2D intensity data were reduced to 1D data as a function of q. Solvent scattering (of water) was rescaled and subtracted from the sample by minimizing the water peak that appears in both the background and the sample at $q \sim 2$ $Å^{-1}$. The reduced data were then further fit by the five-layer core−shell disc (5LCSD, Section 1 in the Supporting Information) or core three-shell sphere (C3SS, Section 2 in the Supporting Information) model provided by SASView 4.2.1 with an invariant ρ_{water} = 9.47 × 10^{-6} $Å^{-2}$, where ρ is the scattering length density (SLD); a fixed rim thickness (t_{rim}) of 10 Å; and a fixed ρ_{rim} = 9.70 × 10^{-6} $Å^{-2}$.[49]

https://doi.org/10.1021/acsami.5c11189
ACS Appl. Mater. Interfaces 2025, 17, 66221−66234

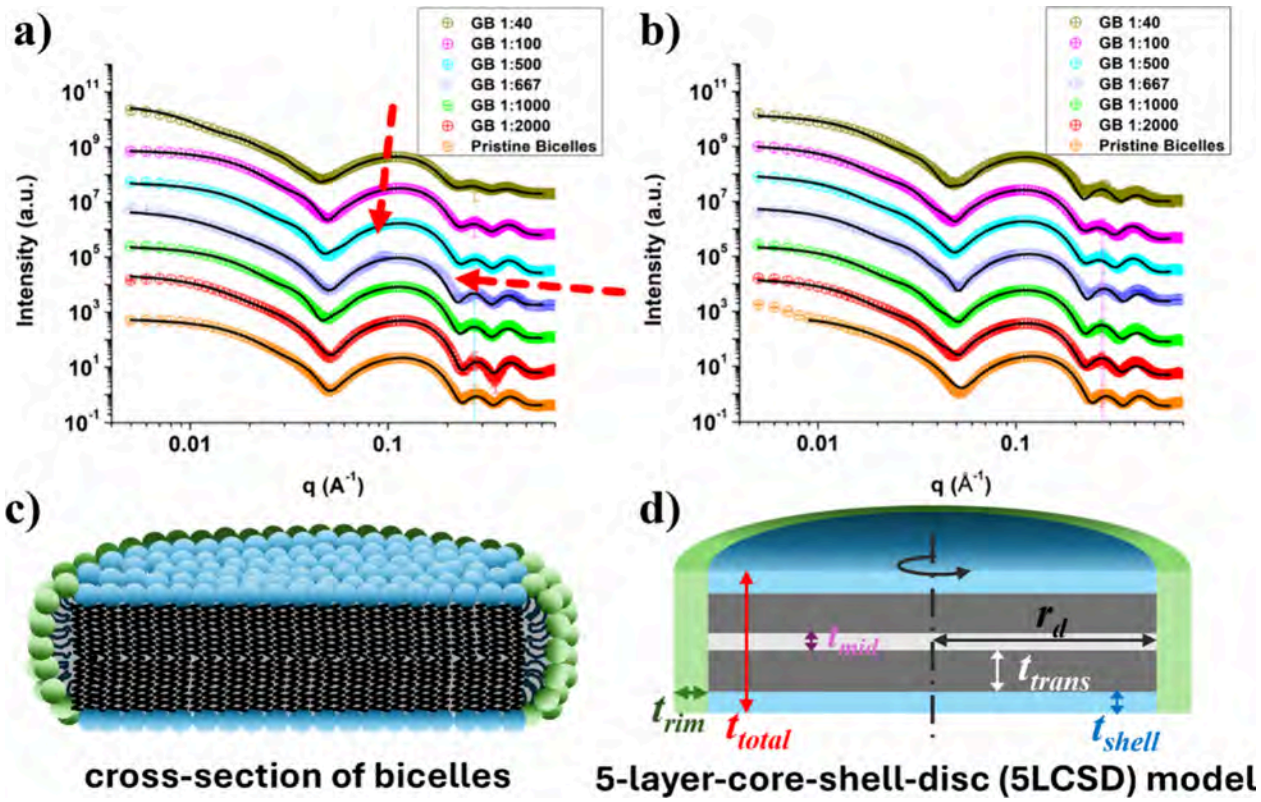

Figure 2. SAXS 5LCSD model fitting results of 1 w/v% (a) low-charge pristine bicelles and GBs (R = 0.01) and (b) high-charge pristine bicelles and GBs (R = 0.05). Red arrows indicate the characteristic MLV peaks. (c) Schematics (cross-sectional view) of the bicelle and (d) 5LCSD model used to fit the SAXS data. The bicelle shows that majority of the long- (blue headgroup) and short- (green headgroup) chain lipids form a planar portion and rim of the disc, respectively. The 5LCSD model indicates the individual regions with distinct electron densities by color and their dimensions.

RESULTS AND DISCUSSION

Structural Analysis. Graphene was prepared by the sonication of graphite in the organic solvent NMP. The resultant graphene dispersion was then centrifuged to remove any unexfoliated graphite and larger graphene flakes as previously demonstrated by Cunning et al.[50] Two populations of hydrodynamic radius (R_H) of the exfoliated graphene were observed by DLS (Figure S2a), suggesting that centrifugation did not remove all larger graphite aggregates. This study focuses on particles with a $R_H \sim 10$ nm, which is similar to the size of bicelles,[14,15,22,24,35,36,51] which are more promising for efficient encapsulation. UV−visible absorbance spectroscopy was performed to obtain the concentration of the graphene dispersion (Figure S2b). Using the previously reported absorbance coefficient of 2460 mL mg^{-1} m^{-1} at 660 nm, the concentration is estimated to be 0.05 mg/mL based on the assumption that majority of the dispersed material is graphene.[52]

Bicelles can robustly self-assemble by simple hydration of the dried lipids in the presence and absence of a hydrophobic payload.[13−16,20−22,24−26,53−56] GB was prepared in the same manner, where dried samples were made by direct addition of aliquots of the graphene dispersion into the lipid mixture followed by removal of the NMP solvent (see Sample Preparation in the Experimental Methods section). The GB mixture was then rehydrated in aqueous solution and thermocycled above and below the melting transition temperature of DPPC ($T_{m,\,DPPC}$ = 41 °C) several times to produce GB.

Figure 1a,b shows the R_H distribution functions of 0.1 w/v% bicelles and GB obtained via DLS measurements. The histograms represent volume-weighted distributions, which are derived from the intensity-weighted distributions based on the approximate scattering intensity from spheres of the corresponding R_H. The peaks of R_H of all samples are in the range between 4 and 20 nm with little or no population of large particles (>100 nm). This outcome agrees well with the distribution function of R_H of the discoidal bicelles reported in the literature.[51] Both low-charge (R = 0.01) and high-charge (R = 0.05) systems form bicelles with slightly increased R_H values upon the incorporation of graphene.

Figure 1c,d shows the physical appearances of C_{lp} = 1.0 w/v % pristine bicelles and GB solutions at two temperatures: above (60 °C) and below (room temperature) $T_{m,DPPC}$. The R = 0.01 pristine bicelles and GB 1:1000 become translucent upon heating, indicative of multiple scattering from large particles (presumably large multilamellar vesicles as reported previously[43,57,58]). The high graphene content sample, GB 1:40, has a brownish color due to solubilized graphene and does not show the same degree of opaqueness at either room temperature or 60 °C, suggesting that graphene loading inhibits the coalescence of the GB, consistent with MD simulations and the observed DSC outcomes discussed below. Similarly, all R = 0.05 GB samples also do not exhibit obvious opaqueness at the two examined temperatures, suggesting that enhanced charge density inhibits the coalescence between particles in good agreement with previous reports[51,56,59] and consistent with the DSC outcomes outlined below.

https://doi.org/10.1021/acsami.5c11189
ACS Appl. Mater. Interfaces 2025, 17, 66221−66234

Table 1. SAXS 5LCSD Best Fitting Results of 1% w/v Pristine Bicelles and GBs with R = 0.01

	pristine bicelles	GB 1:2000	GB 1:1000	GB 1:667	GB 1:500	GB 1:200	GB 1:40
r_d(Å)	139 ± 1	176 ± 1	159 ± 1	174 ± 2	182 ± 1	144 ± 1	328 ± 3
t_{shell}(Å)	10.6 ± 0.3	11.0 ± 0.2	10.7 ± 0.2	10.5 ± 0.3	10.8 ± 0.2	9.6 ± 0.1	9.3 ± 0.2
t_{trans}(Å)	13.0 ± 0.7	12.9 ± 0.6	12.4 ± 0.4	13.8 ± 0.8	14.0 ± 0.3	15.2 ± 0.1	16.4 ± 0.2
t_{mid}(Å)	6.7 ± 1.7	6.3 ± 1.5	8.9 ± 1.1	6.7 ± 2.1	4.6 ± 0.6	4.0 ± 0.1	1.4 ± 0.3
t_{total} (Å)	53.9 ± 3.7	54.1 ± 3.1	55.1 ± 2.3	55.3 ± 4.3	54.2 ± 1.6	52.6 ± 0.5	52.8 ± 1.1

Table 2. SAXS 5LCSD Best Fitting Results of 1 w/v% Pristine Bicelles and GBs with R = 0.05

	pristine bicelles	GB 1:2000	GB 1:1000	GB 1:667	GB 1:500	GB 1:200	GB 1:40
r_d(Å)	125 ± 1	155 ± 1	160 ± 2	199 ± 1	208 ± 1	207 ± 1	172 ± 1
t_{shell}(Å)	10.4 ± 0.3	11.1 ± 0.2	10.7 ± 0.2	11.1 ± 0.2	10.7 ± 0.3	10.6 ± 0.2	11.0 ± 0.1
t_{trans}(Å)	12.7 ± 0.6	14.3 ± 0.5	14.3 ± 0.5	13.9 ± 0.6	14.2 ± 0.3	15.5 ± 0.3	14.0 ± 0.8
t_{mid}(Å)	6.6 ± 1.5	3.9 ± 1.0	4.4 ± 1.0	4.9 ± 1.4	6.3 ± 0.7	4.4 ± 0.8	5.4 ± 1.7
t_{total}(Å)	52.8 ± 3.3	54.7 ± 2.4	54.4 ± 2.4	54.9 ± 3.0	56.1 ± 1.9	56.6 ± 1.8	55.4 ± 3.5

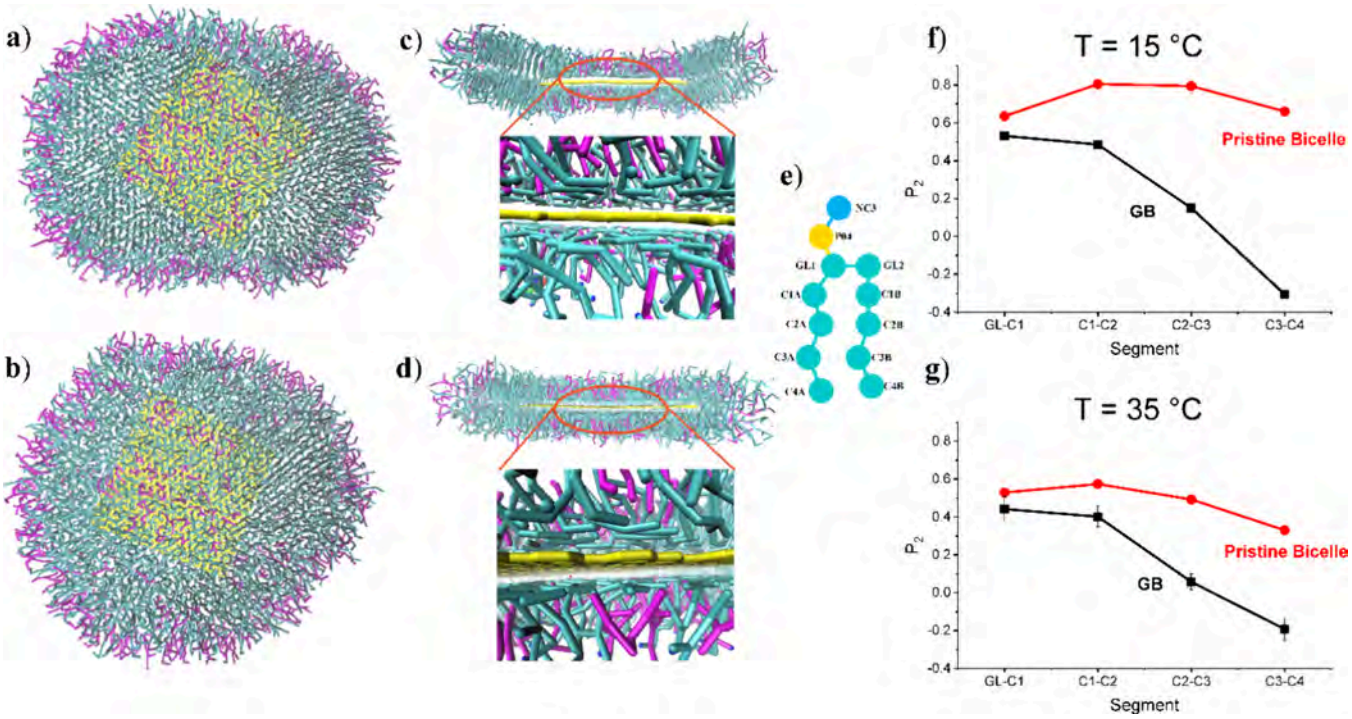

Figure 3. Computer simulation snapshots showing (a) the top view and (c) cross-sectional side view with a zoom-in of the lipids in the vicinity of graphene of a GB equilibrated for 1000 ns at 15 °C and 35 °C (b and d), respectively. DPPC lipids are shown in cyan, DHPC in magenta, and graphene in yellow. Water is not shown for the sake of clarity. (e) Illustration of segment bonds of the coarse-grained DPPC lipid. Segmental order parameter calculated using eq 2 for different segments of DPPC lipids in pristine bicelles and in the vicinity of the graphene in GB at (f) 15 °C and (g) 35 °C.

To further characterize the morphology and internal structure of the nanoparticles, SAXS measurements and analyses were applied to 1.0 w/v% samples. Figure 2a,b showd the SAXS data of both low- (R = 0.01) and high- (R = 0.05) charge mixtures with various graphene contents. Figure 2c describes the possible arrangement of long- and short- chain lipids forming the planar portion and rim of the bicelle. A five-layer core−shell disc (5LCSD) model as shown in Figure 2d was used to obtain the best fit of the data.[49] The five layers include two outer layers of hydrophilic phosphate shells next to two interior layers of an all-trans hydrocarbon regime and an innermost layer of low-density hydrophobic regime (with both trans- and cis- configurations). The fact that all best fits are in good agreement with the SAXS data indicates that the majority of the morphology remains discs. However, in one case (GB 1:667), two weak but observable pseudo-Bragg peaks that appear at q = 0.1 and 0.2 (representing a d-spacing of 62.8 Å), corresponding to a multilamellar vesicle (MLV), are observed as indicated by the red arrows in Figure 2a. It is presumed that the high polydispersity of the graphene size (presumably due to larger graphene fragments) in the initial aliquot may cause vesiculation, and *low-charge systems* at room temperature generally prefer the formation of MLVs for the lower C_{lp} pristine bicellar mixtures.[59] Another possibility is that some of the graphene reaggregates during the hydration step with lipids, leading to the destabilization of a small portion of the bicelles, which transform into MLVs. A similar phenomenon was observed by Raju et al. as graphene was exfoliated in the presence of phospholipids in an aqueous environment.[34] It should be noted that the GBs are stable for at least a week. The

https://doi.org/10.1021/acsami.5c11189
ACS Appl. Mater. Interfaces 2025, 17, 66221−66234

outlier (containing MLVs) can also be rationalized that the centrifugation step might not completely remove all MLVs in the GB 1:667 sample.

The structural parameters of the 5LCSD model include the discoidal radius (r_d), the individual thicknesses of the five layers (accounting for two hydrophilic shells, two all-trans hydrophobic regions, and one trans−cis middle layer denoted by t_{shell}, t_{trans}, and t_{mid}, respectively, as shown in Figure 2d), and the radial thickness of the rim (t_{rim}). The total bilayer thickness (t_{total}) can be described by eq 1.

$$t_{total} = 2t_{shell} + 2t_{trans} + t_{mid} \quad (1)$$

Each region is further defined by a corresponding contrast or scattering length density. The 5LCSD model is further described in Section 1 of the Supporting Information. The best fitting procedure allows us to obtain the bicellar dimensions as reported in Tables 1 (R = 0.01) and 2 (R = 0.05). The best-fit r_d increases upon encapsulating graphene, consistent with the DLS outcomes and reports in the literature.[16,22,24,26] However, r_d does not strongly correlate with graphene content. The largest best-fitting r_d is found in the low-charge sample with the highest graphene content, GB 1:40, reflected by the increasing intensity at low q. Despite the changes observed in individual layer thicknesses (i.e., t_{shell}, t_{trans}, and t_{mid}), t_{total} is conserved for all samples with different graphene contents, in agreement with computer simulation findings discussed next. The bilayer thickness in the range of 53 and 56 Å is within statistical errors (Table 1) and in good agreement with a literature report for pristine bicelles.[49] The decreased t_{mid} value with increased graphene content observed in the low-charge series has the implication that either the large graphene content reduces the gap (the middle layer of trans-/cis- mixing configuration) or it reduces the contrast between the all-trans layers and the midlayer. The latter may be the case as computer simulations discussed below indicate significant lipid reorganization in the presence of graphene. For R = 0.05 GBs, no significant changes are found in any bicellar dimensions.

Molecular Dynamics Simulations. To further understand the interaction between graphene and lipids and assess lipid properties in the vicinity of graphene, CGMD simulations were performed to evaluate the bilayer thickness, lipid order, and lipid mobility. In the CGMD simulations, the bicelle readily formed around a graphene sheet as expected due to the hydrophobicity of lipid tails and hydrophilicity of lipid heads (Figure 3a−d), in good agreement with the previous literature[60] and our experimental outcomes. Computer simulation snapshots of the GB at low (15 °C) temperature (Figure 3a) reveal an oval disc-like shape of the bicelle in contrast to a circular disc shape observed for the pristine bicelle (see Figure S3) at the same temperature or GB at high (35 °C) temperature (Figure 3b). The observed difference in the self-assembled structure originates from the different lipid packing in the presence of graphene at a low temperature and the decreasing lipid order with a temperature increase. To test this hypothesis, we calculated the orientational (second) order parameter using eq 2:

$$P_2 = \frac{3}{2} < \cos^2 \varphi > - \frac{1}{2} \quad (2)$$

where φ is the angle between the bond vectors C4−C3, C3−C2, C2−C1, C1−GL of DPPC lipids (Figure 3 e−g) and the normal to the bicelle. The orientational order parameter can vary from 1 to −0.5, where a value of 1 corresponds to perfect order and a value close to 0 means no order. For a given bond vector, we averaged over the two lipid tails, between different lipids, and also performed a time average using the last 25 ns of the simulation trajectory data. For the pristine bicelle, for the calculation, we used all DPPC lipids except for the bicelle edge, while for GB, we performed averaging over the lipids in the vicinity of graphene, also excluding graphene edges.

As is seen from Figure 3f, at low temperature (15 °C), the pristine bicelle maintains a high lipid order ∼0.65−0.80 for all bond vectors of the DPPC lipid tails. In contrast, DPPC lipids in GB exhibit less order in the vicinity of graphene: P_2 ∼0.45 for GL−C1 and C1−C2 bonds, ∼0.2 for C2−C3, and only about ∼−0.3 for C3−C4 bond at the same temperature (15 °C). The low bond order parameter for the lipid tails is due to the bending of the C3−C4 bond, as seen in the computer simulation snapshot shown in Figure 3c. Indeed, as seen in Figure 3c,d, the thickness of the bicelle is lower in the vicinity of graphene than at other regions, which is due to the bending and orientation along the graphene plane of the DPPC tails located near the graphene. Since lipids tend to maintain a uniform headgroup-to-headgroup bilayer distance throughout the entire bicelle, lipids in the graphene-containing region bend to accommodate the graphene sheet and avoid an increase in the headgroup-to-headgroup bilayer distance, as will be discussed below. Otherwise, there might be raft formation between the graphene-containing area of the bicelle and the graphene-free regions. Consistent with this hypothesis, shorter-tail DHPC lipids do not bend (Figure 3c). Since DHPC has a much shorter length compared to DPPC, it does not need to bend to maintain an unchanged headgroup-to-headgroup bilayer thickness. At high temperature (35 °C), the lipid order decreases for both pristine and GB bicelles (Figure 3g), with the central segments (GL-C1 and C1−C2) maintaining P_2 ∼0.6 for pristine bicelle and ∼0.4 for GB, while the tails (C3−C4) are more disordered at P_2 ∼0.35 for pristine bicelles and P_2 ∼−0.2 for GB where C3−C4 segments orient along the graphene surface (Figure 3d).

To characterize the temperature effect on the DPPC lipid order, we calculated the overall lipid order by averaging the order parameters calculated for all lipid segments (C4−C3, C3−C2, C2−C1, C1−GL), among different lipids, and performing a time average. The results for the DPPC lipid order in pristine and GB bicelles are shown in Figure 4a as a function of temperature. As is seen, in pristine bicelles, the orientational order parameter for DPPC lipids remains about 0.72 until the temperature reaches around 32 °C, when it suddenly declines to below 0.5. This indicates the loss of liquid crystalline order of the lipids and a transition from the gel to a disordered lipid state. This temperature is consistent with previous CGMD studies (using the MARTINI force field) for pure DPPC lipids bilayers[41,42] but smaller than observed experimentally, 41 °C,[36,40] due to the coarse-grained representation of the system in simulations, as discussed above. In contrast, for GB, the DPPC lipid order in the vicinity of graphene remains rather low, around 0.2, at all temperatures studied. This lower lipid order originates from the bending of the lipid tails near the graphene surface, as discussed above (Figure 3). As a result, the temperature is generally found to have a minimal influence on the order of lipids around graphene. It should be noted that, on average, lipids in the vicinity of graphene maintain the initial 3:1 ratio of DPPC/DHPC (Table S1) likely due to slow lipid diffusion in this

https://doi.org/10.1021/acsami.5c11189
ACS Appl. Mater. Interfaces 2025, 17, 66221−66234

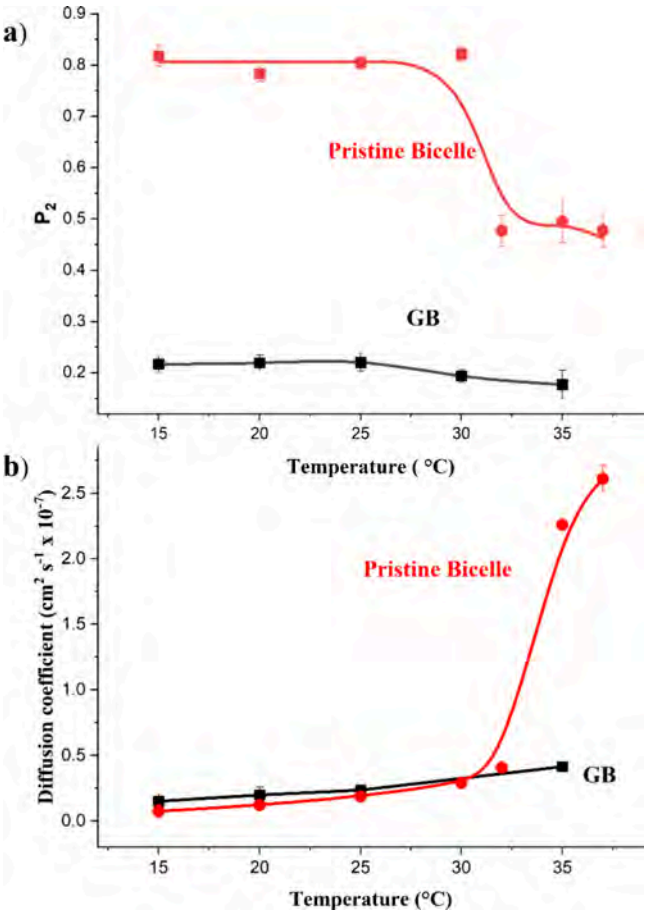

Figure 4. (a) Average orientational order parameter calculated using eq 2 for DPPC lipids in a pristine bicelle (red circles) and in GB in the vicinity of the graphene (black squares) as a function of temperature. (b) Average diffusion coefficient of DPPC lipids in pristine bicelles (red circles) and in GB in the vicinity of the graphene (black squares) as a function of temperature. Lines are guides for the eye only.

region, as discussed below. We have also analyzed the lipid order in the graphene-free regions of GB (Table 3) and found

Table 3. Orientational Order Parameter Calculated Using Eq 2 for DPPC Lipid in Pristine Bicelle and in GB in the Graphene Vicinity and Away from It

temp (°C)	pure lipids in pristine bicelle	graphene-vicinity region of GB	graphene-free region of GB
15	0.82 ± 0.020	0.22 ± 0.016	0.59 ± 0.010
20	0.78 ± 0.015	0.22 ± 0.015	0.53 ± 0.022
25	0.78 ± 0.013	0.22 ± 0.017	0.55 ± 0.014
35	0.50 ± 0.041	0.18 ± 0.028	0.39 ± 0.033

that it is higher than that in the graphene vicinity but lower than that in pristine bicelles. Furthermore, a decrease in lipid order was observed with increasing temperature in the graphene-free regions, similar to that in pristine bicelles, unlike the nearly invariant lipid order in the vicinity of graphene.

Lower lipid order parameters typically indicate that lipids are more likely to be in a disordered phase with a concomitant increased mobility. Since the presence of graphene decreases the lipid order, this could suggest that the lipid mobility might be greater in GB than in pristine bicelles. Lipid mobility is related to the lateral diffusion coefficient, with a higher diffusion coefficient indicating that lipids have more freedom to move within the bicelle. Therefore, lipid mobility was assessed by calculating the lateral diffusion coefficients for the DPPC lipids in pristine and GB bicelles in the vicinity of graphene (Figure 4b). To this end, we first analyzed (using *gmx msd* of GROMACS[47]) the lateral mean square displacement of DPPC lipids using the last 25 ns of the simulation trajectory. The diffusion coefficient D was then calculated from the least-squares fitting of the mean square displacement (Figure S4) using the equation $\lim_{t\to\infty} \langle \|r_i(t) - r_i(0)\|^2 \rangle = 4Dt$. The calculated diffusion coefficients are plotted in Figure 4b as functions of temperature. The diffusion coefficient of DPPC in pristine bicelle systematically increases with temperature and then undergoes a sudden increase around 32 °C when the lipid order decreases and the transition from an ordered (gel) to a disordered (fluid) lipid state occurs. The lateral diffusion coefficient of DPPC is consistent with that previously reported experimentally and in computer simulations: in the gel phase, the diffusion coefficient is in the range of 0.005−0.1× 10^{-7} cm^2 s^{-1} as reported in computer simulations[38,41] and 0.0004−0.16 × 10^{-7} cm^2 s^{-1} measured experimentally,[61] which overlaps with our calculated values of 0.075−0.188 × 10^{-7} cm^2 s^{-1} (Figure 4(b); in the liquid phase, the DPPC diffusion coefficient is in the range of 1−4 × 10^{-7} cm^2 s^{-1} as reported in computer simulations[38,41,62] and 0.6−2 × 10^{-7} cm^2 s^{-1} measured experimentally,[63,64] with our results of ∼2.3 × 10^{-7} cm^2 s^{-1} being within the range of reported values. At lower temperatures (in the gel state), the lipids are tightly packed and their mobility is limited, while at a higher temperature (fluid phase), they move with more freedom. In contrast, the diffusion coefficient of DPPC lipids remains practically unchanged in the vicinity of graphene in GB, indicating that the presence of graphene significantly slows the lipid mobility. This is not surprising considering that, in the vicinity of graphene, DPPC C3−C4 tail segments bend and orient along the graphene (Figure 3), as discussed above. Having such tight contact with graphene anchors the lipids, slowing their diffusion despite their disordered state. Similar observations have been previously reported in the computer simulation literature[33] and experimentally measured for lipid diffusion coefficients on graphene sheets.[65]

We also analyzed the radial distribution function (rdf) for the DPPC and DHPC lipid headgroups (NC3, a coarse-grained atom), which allows us to estimate the bilayer thickness (Figure S5). The first peak of the rdf plot is related to the presence of the nearest neighbors, while the location of the shallow peak at a larger distance gives the thickness of the lipid bilayer in a pristine or graphene-containing bicelle. For a pristine bicelle, we obtained 5.04 ± 0.18 nm thickness at 15 °C (Table 4), in excellent agreement with the experimental data in Table 1 and literature data.[66] For GB, the rdf for the NC3 headgroups was calculated for the lipids located in the vicinity of graphene. We found that the thickness of the bilayer containing a graphene sheet was somewhat smaller, 4.24 ± 0.71 nm, than that in a pristine bicelle (but the statistical error increased due to a smaller statistical sample). This is consistent with the visual observations in Figure 3f, where the tails of DPPC lipids bend in the presence of graphene, leading to a decrease in the bilayer thickness. Figure 3 shows that the C3−C4 bond is frequently bent (especially in the longer tail) and oriented along the graphene surface. The CG length of the

https://doi.org/10.1021/acsami.5c11189
ACS Appl. Mater. Interfaces 2025, 17, 66221−66234

Table 4. Bilayer Thickness, Area per Lipid, and Average Number of Water Molecules per Lipid within 0.6 nm of DPPC Headgroups in Pristine Bicelle and GB, G2B, and G4B at 15 °C

	thickness (nm)	area per lipid (nm^2)	water molecules per DPPC
pristine bicelle	5.04 ± 0.18	0.55 ± 0.09	2.74 ± 0.09
GB	4.24 ± 0.71	0.59 ± 0.07	3.34 ± 0.09
G2B	4.49 ± 1.20	0.68 ± 0.15	3.84 ± 0.09
G4B	5.27 ± 1.16	0.69 ± 0.11	3.94 ± 0.10

C3−C4 (as well as C1−C2 and C2−C3) bond of the DPPC lipid is about 0.47 nm.[37] Thus, if we account for bending of the C3−C4 bond as well as C1−C2 and C2−C3 bonds in the presence of graphene, then one can expect a reduction of 0.95 nm in the bilayer thickness by summing the change of the projections of bond segments onto the normal. The presence of graphene contributes an additional 0.4 nm to the bilayer thickness. Therefore, we would expect a reduction of 0.56 nm in the bilayer thickness, consistent with results obtained from the rdf (Table 4), which however was not detected in the SAXS best fitting results (Table 1) possibly due to the presence of the layered graphene increasing the gap between two leaflets, resulting in thickening the bilayer as will be discussed below. Bending of the lipid tails causes an increased area per lipid from 0.55 to 0.59 nm^2, i.e., a less packed lipid layer and hence a lower lipid ordering, as discussed above. For a pristine bicelle, a large area per lipid (>0.67 nm^2) is found in the disordered state above the melting transition (Table S2). An increase in the area per headgroup implies also a less tight packing of lipids (with possible reduction of contrast between the all-trans layers and the midlayer in the SAXS model discussed above) and an increased number of contacts between headgroups and water. Thus, in GB in the vicinity of graphene, a lipid headgroup is on average in contact with 3.3 CG water molecules, while in pristine bicelle, there are about 3 CG water

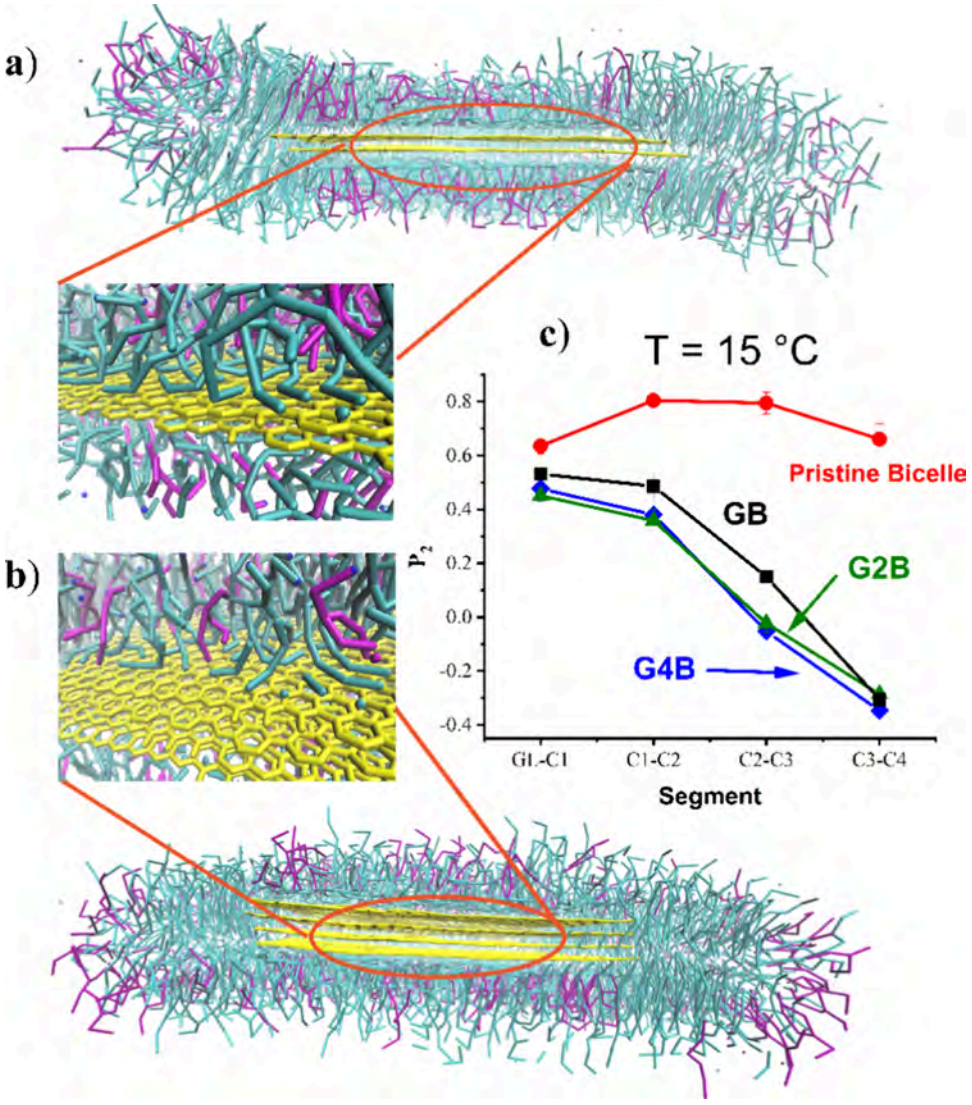

Figure 5. Computer simulation snapshots showing the cross-sectional side view with a zoom-in of the lipids in the vicinity of graphene showing bending of C3−C4 and C2−C3 segments of lipid tails of (a) G2B and (b) G4B equilibrated for 1000 ns at 15 °C. (c) Segmental order parameter for DPPC lipids for pristine bicelles (red squares) and GB containing one graphene (GB black squares), two graphene (G2B green triangles), and four graphene sheets (G4B blue diamonds) at 15 °C. Lines are guides for the eye only.

https://doi.org/10.1021/acsami.5c11189
ACS Appl. Mater. Interfaces 2025, 17, 66221−66234

molecules per lipid headgroup, a result that agrees with 10−12 tightly bound water molecules reported in the literature.[57]

To investigate the effect of layered graphene sheets entrapped in bicelles, we modeled in MD simulations GBs containing a stack of two graphene sheets (G2B) or four graphene sheets (G4B), as shown in Figure 5. Similar to what is seen for a single graphene sheet (Figure 3), bending of lipid tails is observed in the vicinity of graphene stacks with an overall lipid order decrease compared to that of pristine bicelles. Furthermore, analysis of the rdf plot for lipid headgroups (NC3, a coarse-grained atom, see Figure S6) shows that the bilayer thickness changes in a nonmonotonic manner (Table 4). Indeed, for G2B, the bilayer thickness is about 4.49 ± 1.20 nm, which is slightly larger than that for GB, as now the bilayer has to accumulate two graphene sheets inside, which would contribute an extra 0.4 nm consistent with the reported 0.335 nm separation distance between the graphene sheets.[46] A close inspection of lipid organization in the vicinity of the graphene stack shows that the last C3−C4 segment not only of the longer tail but also of the shorter tail and the preceding C2−C3 (and C1−C2) bonds are more bent, which reduce the bilayer thickness in G2B compared to GB by 0.135 nm including 0.084 nm due to the extra bending of C2−C3 bonds and 0.05 nm due to the further bending of C1−C2 bonds. Counting the additional 0.4 nm in the thickness contributed by an extra layer of graphene, the total increase in the bicelle thickness is expected to be 0.4−0.135 = 0.265 nm, which is in an agreement with the 0.25 nm increase according to Table 4. Furthermore, the area per headgroup and contacts with water also increase for G2B compared to GB, indicating that additional changes in the lipid structure to accommodate the second graphene were noticeable. For the stack of four graphene sheets, the thickness of the lipid bilayer increased to 5.27 nm, exceeding that for the pristine bilayer (Table 4). This is not surprising as four graphene sheets added an estimated 1.6 nm to the pristine bilayer or extra 0.8 nm compared to G2B based on two extra separation distances of 0.4 nm between graphene sheets. To compensate for this thick graphene layer (Figure 5b), not only the C3−C4 segment of the longer tail of DPPC but also that of the shorter lipid tail starts to orient more along the graphene surface (Figure 5c), which reduces the bilayer thickness by 0.063 nm that in turn results in an overall increase in the bilayer thickness in G4B compared to G2B by 0.8−0.063 = 0.74 nm, in agreement with the 0.78 nm increase in Table 4 and consistent with experimental data (Table 1). This suggests that the entrapment of graphene sheets may not always change the total bilayer thickness depending on stacking of the entrapped graphene. We also calculated the average area per lipid and number of water molecules per lipid within 0.6 nm of lipid heads for lipids in the vicinity of graphene. On average, for G4B, the area per headgroup increases to 0.69 nm^2, and the number of water molecules per headgroup is about four CG water molecules (Table 4). An increase in the area per lipid and water contact in the presence of graphene may imply a more open lipid layer structure and higher susceptibility to penetration.

Thermal Analysis. DSC thermograms allow us to understand the interior configuration of the hydrocarbon chains better. Figure 6a reveals the thermograms (at a scan rate of 2 °C/min) of the low-charge (R = 0.01) pristine bicelles having an asymmetric peak with its maxima located at 42 °C. This asymmetric peak was convoluted by two thermal events, namely, the main transition of DPPC at roughly $T_{m,DPPC}$ (~42

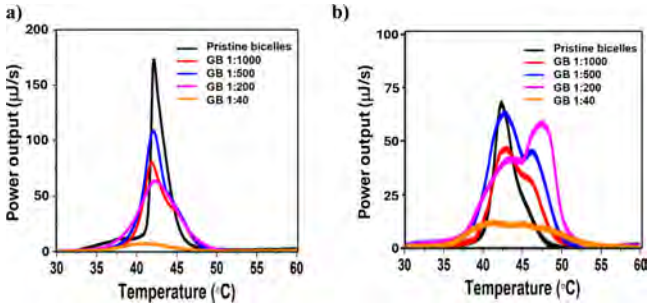

Figure 6. DSC heat scan thermograms of 0.1 w/v% pristine bicelles and GBs at (a) R = 0.01 and (b) R = 0.05 at a heat scan rate of 2 °C/min.

°C) and a structural transformation from bicelle to vesicle (B-to-V) taking place at a slightly higher T (43−45 °C).[53] The encapsulation of graphene in the R = 0.01 series effectively broadens the DPPC main transition. The two peaks are simulated with the sum of two Gaussian peaks, as shown in Figure S7. The first peak (T_1, corresponding to the DPPC main melting/order-to-disorder transition) does not show any dependence of the graphene content (Table 5), while the

Table 5. Enthalpy Values Were Obtained from DSC Heat Thermograms at a 2 °C/min Scan Rate[a]

sample	charge	ΔH_1 (kJ/mol)	ΔH_2 (kJ/mol)	ΔH_{total} (kJ/mol)
pristine bicelles	R = 0.01	6.94 (42.2 ± 0.2 °C)	20.39 (43.1 ± 0.2 °C)	27.33
GB 1:1000		14.82 (41.9 ± 0.3 °C)	8.19 (44.9 ± 0.5 °C)	23.01
GB 1:500		22.86 (**42.1 ± 0.2 °C**)	6.33 (**45.3 ± 0.3 °C**)	29.18
GB 1:200		21.94 (**42.4 ± 0.5 °C**)	2.92 (**45.2 ± 0.4 °C**)	24.86
GB 1:40		N/A	N/A	2.55
pristine bicelles	R = 0.05	10.79 (**42.4 ± 0.3 °C**)	5.76 (**44.8 ± 0.4 °C**)	16.56
GB 1:1000		11.01 (**42.6 ± 0.3 °C**)	6.67 (**46.1 ± 0.3 °C**)	17.67
GB 1:500		20.22 (**42.6 ± 0.3 °C**)	8.05 (**47.0 ± 0.2 °C**)	28.27
GB 1:200		19.29 (**43.2 ± 0.4 °C**)	10.37 (**47.8 ± 0.3 °C**)	29.67
GB 1:40		N/A	N/A	8.65

[a]Peak positions highlighted in bold font.

second peak (T_2, corresponding to the structural transformation) increases with the graphene content of the GB. We have also analyzed the enthalpy of the individual peaks, yielding 6.94 and 20.39 kJ/mol for the first peak (ΔH_1) and the second peak (ΔH_2), respectively, in the case of pristine bicelle, while the GB samples show increased ΔH_1 and decreased ΔH_2 with increased graphene content. The broadened transition peak and enhanced ΔH_1 indicate that the encapsulation of graphene, despite increasing the disordered state of DPPC, elevates the required energy to transform the DPPC from a "restricted liquid-ordered" to a "mobile liquid-disordered" phase. The reduced ΔH_2 with graphene content suggests less energy required to complete the B-to-V transformation. Unexpectedly, the highest graphene content, GB 1:40, where both ΔH_1 and ΔH_2 are negligible, indicates that most DPPC molecules are already in the liquid-

https://doi.org/10.1021/acsami.5c11189
ACS Appl. Mater. Interfaces 2025, 17, 66221−66234

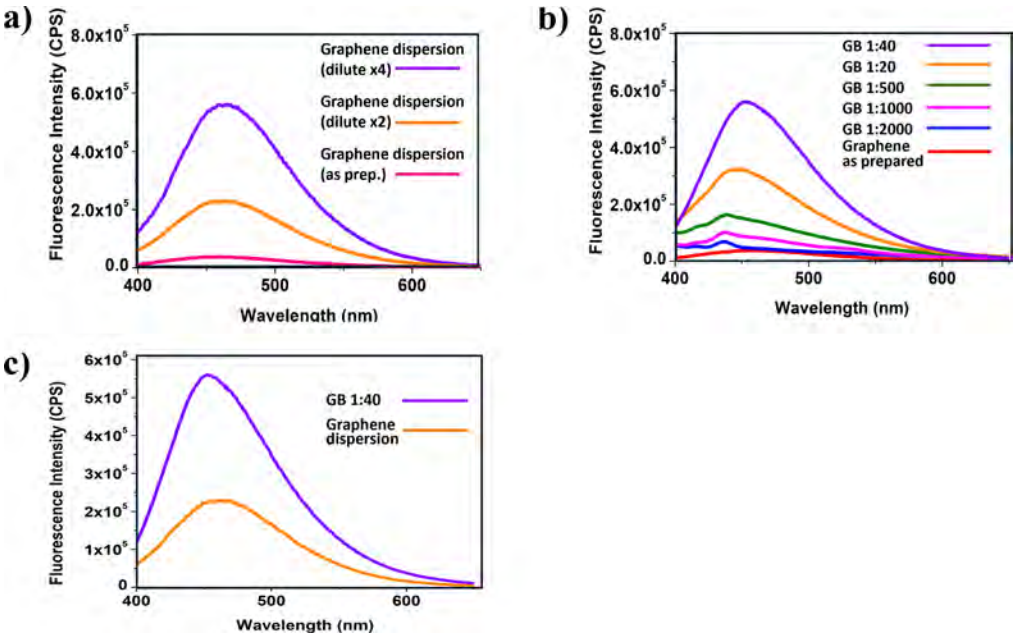

Figure 7. Fluorescence emission spectra of (a) graphene dispersions in NMP (0.05, 0.025, and 0.0125 mg/mL); (b) GBs 1:40, 1:200, 1:500, 1:1000, and 1:2000 and as-prepared graphene dispersion in NMP (0.05 mg/mL); and (c) graphene dispersion 0.025 mg/mL and GB with the same graphene concentration.

disordered phase, as well as a lower energy barrier for the B-to-V transformation.

The outcome for highly charged (R = 0.05) samples as shown in Figure 6b indicates that the transition of highly charged (R = 0.05) pristine bicelles seems to span a wider temperature range than that of the lower charged (R = 0.01) one, presumably attributed to delay of the B-to-V transformation peak taking place at a higher T (~44.8 °C). This is expected as the higher Coulombic repulsion of the R = 0.05 system delays the coalescence of the bicelles.[51,56]

For the R = 0.05 series (except for GB 1:40), a mild increase in ΔH_1 is observed with increased graphene content (10.79 to ~20 kJ/mol), which plateaus beyond GB 1:500 (~20 kJ/mol) for the same reason as described in the R = 0.01 series. Contrary to the R = 0.01 system, the R = 0.05 bicelles show increases in ΔH_2 from 5.76 kJ/mol (pristine bicelle) to 10.37 kJ/mol in GB 1:200, implying a synergistic effect between charge and graphene content. As a result, ΔH_{total} (=ΔH_1 + ΔH_2) increases with increased graphene content (from 16.56 to 29.67 kJ/mol) except for the highest graphene content (GB 1:40), where a rather flat thermogram of the R = 0.05, GB 1:40 samples similar to that of R = 0.01, GB 1:40 is observed. A zoom-in thermogram of the R = 0.05, GB 1:40 sample reveals a few insignificant peaks sitting on a broad background (Figure S8). The drastic decrease of ΔH_{total} (2.55 and 8.65 kJ/mol for R = 0.01 and 0.05, respectively) indicates that overwhelming loading of graphene could induce the DPPC liquid-disordered phase and reduce the barrier of B-to-V structural transformation independent of the charge density of the host bicelles. It has been reported that the formation of stable discoidal bicelles requires sufficient segregation between long- and short-chain lipids, which is normally achieved through temperature control rendering liquid-ordered long-chain and liquid-disordered short-chain lipids, respectively.[36,54−56,59] Apparently, graphene in GB 1:40 samples promotes the disordering of DPPC, consistent with computer simulation results leading to lower barriers for both melting of DPPC and B-to-V transformation.

The enhanced ΔH_1 in GBs (in both R = 0.01 and 0.05 series other than GB 1:40) seems to contradict the diminished segment order parameter, P_2, obtained from MD simulations (Figure 5(c), suggesting more disordered lipid tails in the presence of graphene. This can be rationalized by the fact that the interaction of lipid tails with graphene and the lower mobility of tails due to the inserted graphene (Figure 4b) require higher thermal energy to achieve the true disorder, including increased lipid mobility. It is also reported that polymers entrapped in the bicelle preferably locate at the rim, imposing a strong lateral compression on the planar long-chain lipids.[58] This lends to another explanation that the entrapped smaller graphene may also be located at the fluid rim, leading to greater lateral compression to enhance ΔH_1.

DSC measurements were also performed on the (R = 0.01 and 0.05) GB samples at a higher C_{lp} (1.0 w/v%). Qualitatively similar outcomes (Figure S9) to those of the pristine bicelles are observed. The thermo-induced structural transformation of B-to-V is reversible (i.e., peak corresponding to V-to-B transformation upon cooling) as previously reported in the absence of graphene.[36,53] A sharper order-to-disorder transition peak is found after the first-time thermocycle for R = 0.01 GB series for low GB ratio bicelles as reported in a previous study.[53] However, the R = 0.05 series and R = 0.01, GB 1:40 sample do not show a sharper peak after the first heating process, suggesting that the coalescence of bicelles is suppressed by charge and increased graphene content. The values of ΔH_1 (order-to-disorder transition), ΔH_2 (structural transformation), and ΔH_{tot} (total change of enthalpy) as shown in Table S3 are also independent of graphene content.

SAXS measurements were also conducted on the 1% w/v samples following the thermal pathway: 25 °C → 60 °C → 25 °C. The SAXS data (Figure S10) show the SAXS data of all GB mixtures examined. The scattering models used to best fit the SAXS data are 5LCSD (Section 1 in the Supporting

https://doi.org/10.1021/acsami.5c11189
ACS Appl. Mater. Interfaces 2025, 17, 66221−66234

Information) and the core three-shell sphere (C3SS, Section 2 in the Supporting Information) to describe discoidal and vesicular morphologies at 25 and 60 °C, respectively (Table S4). The best fitting outcomes agree with the corresponding SAXS data well, confirming the DSC results and sample appearance: (1) B-to-V transformation by heating and (2) the structural reversibility (i.e., V-to-B transformation upon cooling). Moreover, the radius of discs grows after the first thermal cycle, consistent with our interpretation on DSC thermograms and a previous report on a dimyristoyl phosphatidylcholine (DMPC)/DHPC/dimyristoyl phosphatidylglycerol (DMPG) bicellar mixture.[62] The analysis of the SAXS data also shows stabilization of the discoidal size in good agreement with the appearance of R = 0.05 GB series (Figure 2b).

Fluorescence Analysis. As pristine graphene does not fluoresce, the fluorescence spectra of the graphene dispersion (in NMP) in Figure 7a shows an unexpected emission peak at ∼460 nm, suggesting that the exfoliation process might cause oxidization of the graphene after the long-time sonication in NMP, but it is also known that sonication of NMP can result in the formation of fluorescent quantum dots.[67] The fact that the fluorescence intensity of the graphene dispersion increases with dilution is a common quenching behavior of fluorophores through either Dexter electron transfer or Förster resonance energy transfer. However, an opposite trend of enhanced emission with graphene concentration was observed in GB samples, where instead of fluorescence quenching, the peak intensity in fact increases with the graphene concentration as shown in Figure 7b. The aggregation-enhanced emission in bicelle-entrapping fluorophores, although unexpected, has been observed for NANO^2-Au nanoclusters[16] and NANO^2-QD (ZnS/ZnSe quantum dots),[26] presumably due to the release of the excitation energy via the emission pathway rather than thermal dissipation as the mobility of the surface ligand of the entrapped nanoparticles is restricted by confinement in the bicelle. The emission was even found to be much higher (>2.5 times) in the case of GB compared to that of free graphene dispersion at the same concentration of graphene. The origin of the emission enhancement is not clear at present but presumably is related to solvatochromism[68] found in carbon nanotubes[69] surrounded by different solvents or restricted mobility of the entrapped graphene sheets.[70] This outcome suggests that bicelles are potential candidates for carrying hydrophobic fluorophores and enhancing their emission efficiency.

CONCLUSIONS

We have successfully demonstrated the formation of stable graphene-loaded bicelles for the first time. Both lipid hosts with lower (R = 0.01) and higher (R = 0.05) charge densities are capable of entrapping graphene without disturbing their discoidal morphology. Our experimental outcomes show that a highly charged GB stabilizes the discoidal morphology through reduced coalescence. The fluorescence of GB shows aggregation-enhanced emission with increased graphene concentration, which is an opposite trend of fluorescence quenching observed in a graphene dispersion in NMP. The radius of bicelles slightly increases upon encapsulation but only weakly depends on the graphene content. A higher graphene content (e.g., GB 1:40) significantly reduces both the "order-to-disorder" and B-to-V enthalpies, suggesting that a good portion of DPPC is already in the disordered phase and thus requires less energy for structural transformation. The detailed analysis of graphene-containing lipid nanodiscs by MD simulations indicates that the presence of graphene significantly disturbs the lipid order as the carbon−carbon bonds of DPPC tails bend to accommodate the entrapped graphene, leading to a significant decrease in the lipid order parameter of the entire bilayer but more so in the vicinity of graphene, in agreement with the proposed premelting of DPPC in the presence of encapsulated graphene based on the DSC data. Despite the fact that segregation of ordered DPPC from disordered DHPC in pristine bicelles plays a crucial role in discoidal stability, the GB disc remains stable even with both DPPC and DHPC being in the disordered phase. MD simulations have also predicted that graphene significantly reduces the lipid mobility in the bicelle, consistent with the broadening and higher enthalpy of the DSC peak for the order-to-disorder transition. In addition to the case of an entrapped single graphene sheet, the bilayer thickness variation is also evaluated by our MD simulations for the cases of multiple graphene sheets (two or four) entrapped in bicelles. These results demonstrate that the bending of lipid tails can in part compensate for the presence of graphene but also results in an increase in the area per lipid and can make the bilayer more susceptible to penetration as the contacts of headgroups with water increase. These research outcomes provide important insights into graphene/lipid interactions as well as structural and dynamic perturbation of the hydrophobic tails of the bilayer. These results suggest that the presence of graphene can significantly impact lipid organization in the bilayer, an effect that must be taken into account in designing graphene-containing nanomaterials intended for biomedical applications or for use in contact with biointerfaces.

ASSOCIATED CONTENT

Supporting Information

The Supporting Information is available free of charge at https://pubs.acs.org/doi/10.1021/acsami.5c11189.

SAXS fitting model details including the five-layered core−shell discoidal model and core three-shell spherical (C3SS) model; computer simulation results and analysis including snapshots of pristine bicelle at low and high temperatures; number of DPPC and DHPC lipids in the graphene-presented region; fitting of diffusion coefficient from the mean square displacement (MSD) plot; bilayer thickness and fitting from the radial distribution function plot; analysis of DSC results including peak fittings for the DSC thermograms; DSC heat scan thermogram; table of enthalpy values obtained from DSC heat thermograms; and SAXS profile and particle size fitted from SAXS before and after heating (PDF)

AUTHOR INFORMATION

Corresponding Authors

Elena Dormidontova − *Polymer Program, Institute of Materials Science and Department of Physics, University of Connecticut, Storrs, Connecticut 06269, United States*; Email: elena@uconn.edu

Mu-Ping Nieh − *Department of Biomedical Engineering, Polymer Program, Institute of Materials Science, Department of Physics, and Department of Chemical & Biomolecular Engineering, University of Connecticut, Storrs, Connecticut*

https://doi.org/10.1021/acsami.5c11189
ACS Appl. Mater. Interfaces 2025, 17, 66221−66234

*06269, United States; orcid.org/0000-0003-4462-8716; Email: mu-ping.nieh@uconn.edu

Authors

Donyeil Hoy, Jr. – *Department of Biomedical Engineering and Polymer Program, Institute of Materials Science, University of Connecticut, Storrs, Connecticut 06269, United States*

Yiyan Kuang – *Polymer Program, Institute of Materials Science and Department of Physics, University of Connecticut, Storrs, Connecticut 06269, United States; orcid.org/0009-0004-2274-7516*

Alemayehu Asres – *Department of Biomedical Engineering, University of Connecticut, Storrs, Connecticut 06269, United States*

Chung-Hao Liu – *Polymer Program, Institute of Materials Science, University of Connecticut, Storrs, Connecticut 06269, United States; orcid.org/0000-0003-1584-0259*

Complete contact information is available at: https://pubs.acs.org/10.1021/acsami.5c11189

Author Contributions

[¥]D.H.J. and Y.K. had equal contribution.

Author Contributions

D.H.J.: prepared samples, designed experiments, analyzed all experimental data, and composed the experimental portion of this manuscript. Y.K.: performed molecular dynamics computer simulation and all analyses of the simulation outcomes and composed the simulation portion of this manuscript. A.A.: prepared samples. C.-H.L.: collected all SAXS data and suggested fitting models. E.E.D.:supervised and provided the strategy of simulation work to align with experimental outcomes and edited the manuscript. M.-P.N.: oversaw the whole project, provided consistent explanations for experimental and simulating outcomes, and proof-read the final manuscript. The manuscript was written through contributions of all authors as described above. All authors have given approval to the final version of the manuscript.

Notes

The authors declare no competing financial interest.

ACKNOWLEDGMENTS

D.H.J. is supported by the US Department of Education GAANN (Award P200A150330), National Science Foundation Graduate Research Fellowship under Grant DGE-1747453, and Giolas-Harriot/Crandall-Cordero and GE fellowships at the University of Connecticut. The authors would like to thank Dr. Douglas Adamson at the University of Connecticut for supplying the graphite. The SAXS data were collected with the help of Dr. Lin Yang at the 16ID-LiX Beamline, National Synchrotron Light Source II, Brookhaven National Laboratory (BNL), NY, USA, through a beamtime proposal (BAG-302208). The LiX beamline is part of the Life Science Biomedical Technology Research resource, jointly supported by the National Institutes of Health, National Institute of General Medical Sciences, under Grant P41 GM111244, and by the Department of Energy Office of Biological and Environmental Research under Grant KP1605010, with additional support from NIH Grant S10 OD012331. NSLS-II is a U.S. Department of Energy (DOE) Office of Science User Facility, operated for the DOE Office of Science by Brookhaven National Laboratory under Contract DESC0012704. This research by Y.K. and Dr. E.E.D. was in part supported by the National Science Foundation under Grant CHE-2004072. The authors would like to thank Jack Conley for designing the cover art for the article.

REFERENCES

(1) Novoselov, K. S.; Geim, A. K.; Morozov, S. V.; Jiang, D.; Zhang, Y.; Dubonos, S. V.; Grigorieva, I. V.; Firsov, A. A. Electric Field Effect in Atomically Thin Carbon Films. *Science* **2004**, *306* (5696), 666–669.

(2) Syama, S.; Mohanan, P. V. Safety and Biocompatibility of Graphene: A New Generation Nanomaterial for Biomedical Application. *Int. J. Biol. Macromol.* **2016**, *86*, 546–555.

(3) Liu, J.; Guo, S.; Han, L.; Wang, T.; Hong, W.; Liu, Y.; Wang, E. Synthesis of Phospholipid Monolayer Membrane Functionalized Graphene for Drug Delivery. *J. Mater. Chem.* **2012**, *22* (38), 20634–20640.

(4) Chong, Y.; Ma, Y.; Shen, H.; Tu, X.; Zhou, X.; Xu, J.; Dai, J.; Fan, S.; Zhang, Z. The in Vitro and in Vivo Toxicity of Graphene Quantum Dots. *Biomaterials* **2014**, *35* (19), 5041–5048.

(5) Yang, K.; Gong, H.; Shi, X.; Wan, J.; Zhang, Y.; Liu, Z. In Vivo Biodistribution and Toxicology of Functionalized Nano-Graphene Oxide in Mice after Oral and Intraperitoneal Administration. *Biomaterials* **2013**, *34* (11), 2787–2795.

(6) Wong-Ekkabut, J.; Baoukina, S.; Triampo, W.; Tang, I.-M.; Tieleman, D. P.; Monticelli, L. Computer Simulation Study of Fullerene Translocation through Lipid Membranes. *Nat. Nanotechnol.* **2008**, *3* (6), 363–368.

(7) Wang, J.; Wei, Y.; Shi, X.; Gao, H. Cellular Entry of Graphene Nanosheets: The Role of Thickness. *Oxidation and Surface Adsorption. RSC Adv.* **2013**, *3* (36), 15776–15782.

(8) Sanders, C. R. I.; Schwonek, J. P. Characterization of Magnetically Orientable Bilayers in Mixtures of Dihexanoylphosphatidylcholine and Dimyristoylphosphatidylcholine by Solid-State NMR. *Biochemistry* **1992**, *31* (37), 8898–8905.

(9) Denisov, I. G.; Sligar, S. G. Nanodiscs for Structural and Functional Studies of Membrane Proteins. *Nat. Struct Mol. Biol.* **2016**, *23* (6), 481–486.

(10) Stroud, Z.; Hall, S. C. L.; Dafforn, T. R. Purification of Membrane Proteins Free from Conventional Detergents: SMA, New Polymers. *New Opportunities and New Insights. Methods* **2018**, *147*, 106–117.

(11) Lee, S. C.; Knowles, T. J.; Postis, V. L. G.; Jamshad, M.; Parslow, R. A.; Lin, Y.; Goldman, A.; Sridhar, P.; Overduin, M.; Muench, S. P.; Dafforn, T. R. A Method for Detergent-Free Isolation of Membrane Proteins in Their Local Lipid Environment. *Nat. Protoc* **2016**, *11* (7), 1149–1162.

(12) Dörr, J. M.; Scheidelaar, S.; Koorengevel, M. C.; Dominguez, J. J.; Schäfer, M.; van Walree, C. A.; Killian, J. A. The Styrene-Maleic Acid Copolymer: A Versatile Tool in Membrane Research. *Eur. Biophys J.* **2016**, *45* (1), 3–21.

(13) Li, M.; Morales, H. H.; Katsaras, J.; Kučerka, N.; Yang, Y.; Macdonald, P. M.; Nieh, M.-P. Morphological Characterization of DMPC/CHAPSO Bicellar Mixtures: A Combined SANS and NMR Study. *Langmuir* **2013**, *29* (51), 15943–15957.

(14) Nieh, M.-P.; Glinka, C. J.; Krueger, S.; Prosser, R. S.; Katsaras, J. SANS Study of the Structural Phases of Magnetically Alignable Lanthanide-Doped Phospholipid Mixtures. *Langmuir* **2001**, *17* (9), 2629–2638.

(15) Nieh, M.-P.; Glinka, C. J.; Krueger, S.; Prosser, R. S.; Katsaras, J. SANS Study on the Effect of Lanthanide Ions and Charged Lipids on the Morphology of Phospholipid Mixtures. *Biophys. J.* **2002**, *82* (5), 2487–2498.

(16) Tahmasbi Rad, A.; Bao, Y.; Jang, H. S.; Xia, Y.; Sharma, H.; Dormidontova, E. E.; Zhao, J.; Arora, J.; John, V. T.; Tang, B. Z.; Dainese, T.; Hariri, A.; Jokerst, J. V.; Maran, F.; Nieh, M. P. Aggregation-Enhanced Photoluminescence and Photoacoustics of Atomically Precise Gold Nanoclusters in Lipid Nanodiscs ($NANO^2$). *Adv. Funct. Mater.* **2021**, *31* (10), 1–9.

(17) Rubio, L.; Alonso, C.; Rodríguez, G.; Barbosa-Barros, L.; Coderch, L.; De la Maza, A.; Parra, J. L.; López, O. Bicellar Systems for *in Vitro* Percutaneous Absorption of Diclofenac. *Int. J. Pharm.* **2010**, *386* (1), 108−113.
(18) Lucyanna, B.-B.; Gelen, R.; Merce, C.; Laia, R.; Carmen, L.-I.; Alfons, D. la M.; Olga, L. Structural Versatility of Bicellar Systems and Their Possibilities as Colloidal Carriers. *Pharmaceutics* **2011**, *3* (3), 636−664.
(19) Fernández, E.; Rodríguez, G.; Cócera, M.; Barbosa-Barros, L.; Alonso, C.; López-Iglesias, C.; Jawhari, T.; de la Maza, A.; López, O. Advanced Lipid Systems Containing β-Carotene: Stability under UV-Vis Radiation and Application on Porcine Skin in Vitro. *Phys. Chem. Chem. Phys.* **2015**, *17* (28), 18710−18721.
(20) Lin, L.; Liang, X.; Xu, Y.; Yang, Y.; Li, X.; Dai, Z. Doxorubicin and Indocyanine Green Loaded Hybrid Bicelles for Fluorescence Imaging Guided Synergetic Chemo/Photothermal Therapy. *Bioconjugate Chem.* **2017**, *28* (9), 2410−2419.
(21) Tahmasbi Rad, A.; Chen, C.-W.; Aresh, W.; Xia, Y.; Lai, P.-S.; Nieh, M.-P. Combinational Effects of Active Targeting, Shape, and Enhanced Permeability and Retention for Cancer Theranostic Nanocarriers. *ACS Appl. Mater. Interfaces* **2019**, *11* (11), 10505−10519.
(22) Tahmasbi Rad, A.; Malik, S.; Yang, L.; Oberoi-Khanuja, T. K.; Nieh, M. P.; Bahal, R. A Universal Discoidal Nanoplatform for the Intracellular Delivery of PNAs. *Nanoscale* **2019**, *11* (26), 12517−12529.
(23) Belling, J. N.; Heidenreich, L. K.; Park, J. H.; Kawakami, L. M.; Takahashi, J.; Frost, I. M.; Gong, Y.; Young, T. D.; Jackman, J. A.; Jonas, S. J.; Cho, N.-J.; Weiss, P. S. Lipid-Bicelle-Coated Microfluidics for Intracellular Delivery with Reduced Fouling. *ACS Appl. Mater. Interfaces* **2020**, *12* (41), 45744−45752.
(24) Rad, A. T.; Hargrove, D.; Daneshmandi, L.; Ramsdell, A.; Lu, X.; Nieh, M.-P. Codelivery of Paclitaxel and Parthenolide in Discoidal Bicelles for a Synergistic Anticancer Effect: Structure Matters. *Advanced NanoBiomed Research* **2022**, *2* (1), No. 2100080.
(25) Aresh, W.; Liu, Y.; Sine, J.; Thayer, D.; Puri, A.; Huang, Y.; Wang, Y.; Nieh, M.-P. The Morphology of Self-Assembled Lipid-Based Nanoparticles Affects Their Uptake by Cancer Cells. *J. Biomed Nanotechnol* **2016**, *12* (10), 1852−1863.
(26) Fang, J. M.; Basu, S.; Li, M.; Shih, K. C.; Wang, J.; Cotlet, M.; Wang, X.; Zhao, J.; Mountziaris, T. J.; LoTurco, J. J.; Nieh, M. P. Restriction-In-Motion of Surface Ligands Enhances Photoluminescence of Quantum Dots—Experiment and Theory. *Advanced Materials Interfaces* **2022**, *9* (6), 1−9.
(27) Bortolus, M.; Parisio, G.; Maniero, A. L.; Ferrarini, A. Monomeric Fullerenes in Lipid Membranes: Effects of Molecular Shape and Polarity. *Langmuir* **2011**, *27* (20), 12560−12568.
(28) Titov, A. V.; Král, P.; Pearson, R. Sandwiched Graphene−Membrane Superstructures. *ACS Nano* **2010**, *4* (1), 229−234.
(29) Guo, R.; Mao, J.; Yan, L.-T. Computer Simulation of Cell Entry of Graphene Nanosheet. *Biomaterials* **2013**, *34* (17), 4296−4301.
(30) Chen, J.; Zhou, G.; Chen, L.; Wang, Y.; Wang, X.; Zeng, S. Interaction of Graphene and Its Oxide with Lipid Membrane: A Molecular Dynamics Simulation Study. *J. Phys. Chem. C* **2016**, *120* (11), 6225−6231.
(31) Li, Z.; Zhu, X.; Li, J.; Zhong, J.; Zhang, J.; Fan, J. Molecular Insights into the Resistance of Phospholipid Heads to the Membrane Penetration of Graphene Nanosheets. *Nanoscale* **2022**, *14* (14), 5384−5391.
(32) Tan, B.; Hu, J.; Wu, F. Cholesterols Induced Distinctive Entry of the Graphene Nanosheet into the Cell Membrane. *ACS Omega* **2024**, *9* (8), 9216−9225.
(33) Willems, N.; Urtizberea, A.; Verre, A. F.; Iliut, M.; Lelimousin, M.; Hirtz, M.; Vijayaraghavan, A.; Sansom, M. S. P. Biomimetic Phospholipid Membrane Organization on Graphene and Graphene Oxide Surfaces: A Molecular Dynamics Simulation Study. *ACS Nano* **2017**, *11* (2), 1613−1625.
(34) Raju, A. P. A.; Offerman, S. C.; Gorgojo, P.; Vallés, C.; Bichenkova, E. V.; Aojula, H. S.; Vijayraghavan, A.; Young, R. J.; Novoselov, K. S.; Kinloch, I. A.; Clarke, D. J. Dispersal of Pristine Graphene for Biological Studies. *RSC Adv.* **2016**, *6* (73), 69551−69559.
(35) Khan, U.; O'Neill, A.; Porwal, H.; May, P.; Nawaz, K.; Coleman, J. N. Size Selection of Dispersed, Exfoliated Graphene Flakes by Controlled Centrifugation. *Carbon* **2012**, *50* (2), 470−475.
(36) Liu, Y.; Li, M.; Yang, Y.; Xia, Y.; Nieh, M.-P. The Effects of Temperature, Salinity, Concentration and PEGylated Lipid on the Spontaneous Nanostructures of Bicellar Mixtures. Biochimica et Biophysica Acta (BBA) -. *Biomembranes* **2014**, *1838* (7), 1871−1880.
(37) Marrink, S. J.; Risselada, H. J.; Yefimov, S.; Tieleman, D. P.; De Vries, A. H. The MARTINI Force Field: Coarse Grained Model for Biomolecular Simulations. *J. Phys. Chem. B* **2007**, *111* (27), 7812−7824.
(38) Marrink, S. J.; Risselada, J.; Mark, A. E. Simulation of Gel Phase Formation and Melting in Lipid Bilayers Using a Coarse Grained Model. *Chem. Phys. Lipids* **2005**, *135* (2), 223−244.
(39) Balgavý, P.; Dubničková, M.; Kučerka, N.; Kiselev, M. A.; Yaradaikin, S. P.; Uhríková, D. Bilayer Thickness and Lipid Interface Area in Unilamellar Extruded 1,2-Diacylphosphatidylcholine Liposomes: A Small-Angle Neutron Scattering Study. *Biochim. Biophys. Acta, Biomembr.* **2001**, *1512* (1), 40−52.
(40) Lewis, R. N. A. H.; Mak, N.; McElhaney, R. N. A Differential Scanning Calorimetric Study of the Thermotropic Phase Behavior of Model Membranes Composed of Phosphatidylcholines Containing Linear Saturated Fatty Acyl Chains. *Biochemistry* **1987**, *26* (19), 6118−6126.
(41) Wang, Y.; Gkeka, P.; Fuchs, J. E.; Liedl, K. R.; Cournia, Z. DPPC-Cholesterol Phase Diagram Using Coarse-Grained Molecular Dynamics Simulations. Biochimica et Biophysica Acta (BBA) -. *Biomembranes* **2016**, *1858* (11), 2846−2857.
(42) Yang, L.; Kindt, J. T. Line Tension Assists Membrane Permeation at the Transition Temperature in Mixed-Phase Lipid Bilayers. *J. Phys. Chem. B* **2016**, *120* (45), 11740−11750.
(43) Sharma, H.; Dormidontova, E. E. Lipid Nanodisc-Templated Self-Assembly of Gold Nanoparticles into Strings and Rings. *ACS Nano* **2017**, *11* (4), 3651−3661.
(44) Ruiz, L.; Xia, W.; Meng, Z.; Keten, S. A Coarse-Grained Model for the Mechanical Behavior of Multi-Layer Graphene. *Carbon* **2015**, *82*, 103−115.
(45) Puigpelat, E.; Ignés-Mullol, J.; Sagués, F.; Reigada, R. Interaction of Graphene Nanoparticles and Lipid Membranes Displaying Different Liquid Orderings: A Molecular Dynamics Study. *Langmuir* **2019**, *35* (50), 16661−16668.
(46) Sengupta, R.; Bhattacharya, M.; Bandyopadhyay, S.; Bhowmick, A. K. A review on the mechanical and electrical properties of graphite and modified graphite reinforced polymer composites. *Progress in Polymer Science* **2011**, *36*, 638−670.
(47) Abraham, M. J.; Murtola, T.; Schulz, R.; Páll, S.; Smith, J. C.; Hess, B.; Lindahl, E. GROMACS: High Performance Molecular Simulations through Multi-Level Parallelism from Laptops to Supercomputers. *SoftwareX* **2015**, *1−2*, 19−25.
(48) Humphrey, W.; Dalke, A.; Schulten, K. VMD: Visual Molecular Dynamics. *J. Mol. Graphics* **1996**, *14* (1), 33−38.
(49) Cheu, C.; Yang, L.; Nieh, M.-P. Refining Internal Bilayer Structure of Bicelles Resolved by Extended-*q* Small Angle X-Ray Scattering. *Chem. Phys. Lipids* **2020**, *231*, No. 104945.
(50) Cunning, B. V.; Ishioka, K.; Brown, C. L.; Kielpinski, D. Size-Dependent Hot-Phonon Dynamics in Graphene Flakes. *Appl. Phys. Lett.* **2014**, *104* (18), 181907.
(51) Hu, A.; Fan, T.-H.; Katsaras, J.; Xia, Y.; Li, M.; Nieh, M.-P. Lipid-Based Nanodiscs as Models for Studying Mesoscale Coalescence − a Transport Limited Case. *Soft Matter* **2014**, *10* (28), 5055−5060.
(52) Hernandez, Y.; Nicolosi, V.; Lotya, M.; Blighe, F. M.; Sun, Z.; De, S.; McGovern, I. T.; Holland, B.; Byrne, M.; Gun'Ko, Y. K.; Boland, J. J.; Niraj, P.; Duesberg, G.; Krishnamurthy, S.; Goodhue, R.; Hutchison, J.; Scardaci, V.; Ferrari, A. C.; Coleman, J. N. High-Yield

https://doi.org/10.1021/acsami.5c11189
ACS Appl. Mater. Interfaces 2025, 17, 66221−66234

Production of Graphene by Liquid-Phase Exfoliation of Graphite. *Nat. Nanotechnol.* **2008**, *3* (9), 563−568.
(53) Alahmadi, I.; Hoy, D.; Tahmasbi Rad, A.; Patil, S.; Alahmadi, A.; Kinnun, J.; Scott, H. L.; Katsaras, J.; Nieh, M. P. Changes Experienced by Low-Concentration Lipid Bicelles as a Function of Temperature. *Langmuir* **2022**, *38* (14), 4332−4340.
(54) Liu, Y.; Xia, Y.; Rad, A. T.; Aresh, W.; Fang, J. M.; Nieh, M.-P. Stable Discoidal Bicelles: Formulation, Characterization, and Functions. In *Liposomes: Methods and Protocols*; D'Souza, G. G. M.; Zhang, H., Eds.; Springer US: New York, NY, 2023; pp 147−157. .
(55) Li, M.; Heller, W. T.; Liu, C.-H.; Gao, C. Y.; Cai, Y.; Hou, Y.; Nieh, M.-P. Effects of Fluidity and Charge Density on the Morphology of a Bicellar Mixture − A SANS Study. Biochimica et Biophysica Acta (BBA) -. *Biomembranes* **2020**, *1862* (9), No. 183315.
(56) Mahabir, S.; Small, D.; Li, M.; Wan, W.; Kučerka, N.; Littrell, K.; Katsaras, J.; Nieh, M.-P. Growth Kinetics of Lipid-Based Nanodiscs to Unilamellar Vesicles—A Time-Resolved Small Angle Neutron Scattering (SANS) Study. Biochimica et Biophysica Acta (BBA) -. *Biomembranes* **2013**, *1828* (3), 1025−1035.
(57) Disalvo, E. A.; Lairion, F.; Martini, F.; Tymczyszyn, E.; Frías, M.; Almaleck, H.; Gordillo, G. J. Structural and Functional Properties of Hydration and Confined Water in Membrane Interfaces. Biochimica et Biophysica Acta (BBA) -. *Biomembranes* **2008**, *1778* (12), 2655−2670.
(58) Liu, C.-H.; Cheu, C.; Barker, J. G.; Yang, L.; Nieh, M.-P. Facile Polymerization in a Bicellar Template to Produce Polymer Nano-Rings. *J. Colloid Interface Sci.* **2023**, *630*, 629−637.
(59) Nieh, M.-P.; Dolinar, P.; Kučerka, N.; Kline, S. R.; Debeer-Schmitt, L. M.; Littrell, K. C.; Katsaras, J. Formation of Kinetically Trapped Nanoscopic Unilamellar Vesicles from Metastable Nano-discs. *Langmuir* **2011**, *27* (23), 14308−14316.
(60) Wu, D.; Yang, X. Coarse-Grained Molecular Simulation of Self-Assembly for Nonionic Surfactants on Graphene Nanostructures. *J. Phys. Chem. B* **2012**, *116* (39), 12048−12056.
(61) Lee, B.-S.; Mabry, S. A.; Jonas, A.; Jonas, J. High-Pressure Proton NMR Study of Lateral Self-Diffusion of Phosphatidylcholines in Sonicated Unilamellar Vesicles. *Chem. Phys. Lipids* **1995**, *78* (2), 103−117.
(62) Miguel, V.; Perillo, M. A.; Villarreal, M. A. Improved Prediction of Bilayer and Monolayer Properties Using a Refined BMW-MARTINI Force Field. Biochimica et Biophysica Acta (BBA) -. *Biomembranes* **2016**, *1858* (11), 2903−2910.
(63) Kuo, A.-L.; Wade, C. G. Lipid Lateral Diffusion by Pulsed Nuclear Magnetic Resonance. *Biochemistry* **1979**, *18* (11), 2300−2308.
(64) Lindahl, E.; Edholm, O. Molecular Dynamics Simulation of NMR Relaxation Rates and Slow Dynamics in Lipid Bilayers. *J. Chem. Phys.* **2001**, *115* (10), 4938−4950.
(65) Farell, M.; Wetherington, M.; Shankla, M.; Chae, I.; Subramanian, S.; Kim, S. H.; Aksimentiev, A.; Robinson, J.; Kumar, M. Characterization of the Lipid Structure and Fluidity of Lipid Membranes on Epitaxial Graphene and Their Correlation to Graphene Features. *Langmuir* **2019**, *35* (13), 4726−4735.
(66) Balgavý, P.; Dubničková, M.; Kučerka, N.; Kiselev, M. A.; Yaradaikin, S. P.; Uhríková, D. Bilayer Thickness and Lipid Interface Area in Unilamellar Extruded 1,2-Diacylphosphatidylcholine Liposomes: A Small-Angle Neutron Scattering Study. *Biochim. Biophys. Acta, Biomembr.* **2001**, *1512* (1), 40−52.
(67) Das, S. K.; Gawas, R.; Chakrabarty, S.; Harini, G.; Patidar, R.; Jasuja, K. An Unexpected Transformation of Organic Solvents into 2D Fluorescent Quantum Dots during Ultrasonication-Assisted Liquid-Phase Exfoliation. *J. Phys. Chem. C* **2019**, *123* (41), 25412−25421.
(68) Ascherl, L.; Evans, E. W.; Hennemann, M.; Di Nuzzo, D.; Hufnagel, A. G.; Beetz, M.; Friend, R. H.; Clark, T.; Bein, T.; Auras, F. *Solvatochromic Covalent Organic Frameworks. Nat. Commun.* **2018**, *9* (1), 3802.
(69) Kunai, Y.; Liu, A. T.; Cottrill, A. L.; Koman, V. B.; Liu, P.; Kozawa, D.; Gong, X.; Strano, M. S. Observation of the Marcus Inverted Region of Electron Transfer from Asymmetric Chemical Doping of Pristine (n, m) Single-Walled Carbon Nanotubes. *J. Am. Chem. Soc.* **2017**, *139* (43), 15328−15336.
(70) Hong, Y.; Lam, J. W. Y.; Tang, B. Z. Aggregation-Induced Emission. *Chem. Soc. Rev.* **2011**, *40* (11), 5361−5388.

https://doi.org/10.1021/acsami.5c11189
ACS Appl. Mater. Interfaces 2025, 17, 66221−66234